Article

Nanocrystal-tailored recombination for all-perovskite tandem solar modules

https://doi.org/10.1038/s41586-026-10768-1

Received: 18 November 2025

Accepted: 4 June 2026

Published online: 15 June 2026

Check for updates

Ke Xiao[1,2,3,10]✉, Hongfei Sun[1,10], Xinke Kong[4,10], Han Gao[1,10], Jing Lou[5], Xingze Chen[6], Zimo Hu[7], Dongdong Xu[1], Renxing Lin[1], Runnan Liu[1], Siyu Xia[4,8], Jin Xie[4,8], Ye Liu[2], Xin Luo[2], Fengjia Fan[7], Changqi Ma[6], Chao Chang[5], Yuanyuan Wang[4]✉ & Hairen Tan[1,2,9]✉

The commercialization of all-perovskite tandem solar modules is hindered by the reliance on the conventional gold-based tunnel recombination junction[1,2]. Specifically, this tunnel recombination junction introduces substantial near-infrared parasitic absorption[3] and suffers from interfacial instability[4], limiting both photocurrent generation and operational durability. Here, we develop a solution-processed interconnecting layer based on surface-engineered indium oxide nanocrystals featuring high optical transparency, in which controlled nanocrystal morphology and tailored ligand chemistry enable smooth interfacial contact and favourable energy-level alignment. We introduce a phosphonic acid additive into the lead–tin perovskite precursor, which synergistically improves the electronic contact with the indium oxide recombination layer, thereby enhancing hole extraction. Moreover, the additive regulates perovskite crystallization to mitigate residual strain during film formation, ensuring high-quality large-area deposits. This coordinated interfacial and crystallization engineering strategy simultaneously enhances carrier recombination efficiency at the interconnection layer, improves carrier extraction and promotes large-area film uniformity in all-perovskite tandems. As a result, a 65-cm^2 all-perovskite tandem solar module achieves a certified power conversion efficiency of 26.2% (ref. 5), with an open-circuit voltage of 2.182 V, a fill factor of 77.4% and a short-circuit current density of 15.6 mA cm^{-2} in terms of averaged subcell performance, measured by the Japan Electrical Safety and Environment Technology Laboratories. This marks a notable advance towards scalable perovskite tandem photovoltaics.

All-perovskite tandem solar modules (TSMs) represent a compelling next-generation photovoltaic technology, offering exceptional power conversion efficiency (PCE), cost-effectiveness and scalability for viable commercialization[1,2,6,7]. Although record small-area all-perovskite tandem devices (about 0.1 cm^2) have surpassed 30% efficiency[8], their large-area modules (with area ≥20 cm^2) remain limited to 24.5%, primarily because of insufficient short-circuit current density (J_{SC} < 15 mA cm^{-2} per subcell, whereas the subcell current density is normalized by the area of a single subcell)[2,9,10]. This performance disparity is largely associated with optical and energetic losses in commonly used tunnel recombination junction (TRJ) architectures and is further exacerbated by charge-transport limitations in large-area lead–tin (Pb–Sn) perovskite films during scalable deposition[11–13].

Advanced all-perovskite TSMs typically use a conventional TRJ configuration consisting of an ultrathin gold layer and a poly (3,4-ethylenedioxythiophene)-poly(styrene sulfonate) (PEDOT-PSS) layer atop an atomic-layer-deposited SnO_2 (ALD-SnO_2) film[9,10,14,15]. Although this structure enables efficient carrier recombination and suppresses lateral conductivity to prevent shunting (Supplementary Note 1 and Supplementary Fig. 1), metal-based TRJ can introduce practical challenges during large-area fabrication. In particular, maintaining uniform ultrathin metal films over large substrates is difficult, and even minor inhomogeneities can notably increase optical absorption and impair module efficiency. Furthermore, the use of precious metals raises concerns regarding scalability and manufacturing cost. Meanwhile, although the PEDOT-PSS hole-transport layer provides a deep work function and high conductivity[9,16,17], it introduces substantial parasitic absorption losses and suffers from chemical instability because of its acidic nature[4,18].

To overcome these limitations, various hole-selective materials (HSMs), including metal oxides[19–22], organic compounds[23–26] and self-assembled monolayers (SAMs)[12,27,28], have been explored as

[1]National Laboratory of Solid State Microstructures, College of Engineering and Applied Sciences, Frontiers Science Center for Critical Earth Material Cycling, Nanjing University, Nanjing, China. [2]Research and Development (R&D) Center, Renshine Solar, Suzhou, China. [3]School of Advanced Manufacturing Engineering, Nanjing University, Suzhou, China. [4]State Key Laboratory of Coordination Chemistry, School of Chemistry, Nanjing University, Nanjing, China. [5]Innovation Laboratory of Terahertz Biophysics, National Innovation Institute of Defense Technology, Beijing, China. [6]i-Lab and Printable Electronics Research Center, Suzhou Institute of Nano-Tech and Nano-Bionics, Chinese Academy of Sciences, Suzhou, China. [7]School of Physical Sciences, University of Science and Technology of China, Hefei, China. [8]Jiangsu Key Laboratory of Advanced Organic Materials, Chemistry and Biomedicine Innovation Center (ChemBIC), Nanjing University, Nanjing, China. [9]National Laboratory of Solid State Microstructures, College of Engineering and Applied Sciences, Jiangsu Physical Science Research Center, Nanjing University, Nanjing, China. [10]These authors contributed equally: Ke Xiao, Hongfei Sun, Xinke Kong, Han Gao. ✉e-mail: ke.xiao@nju.edu.cn; wangyy@nju.edu.cn; hairentan@nju.edu.cn

alternatives to PEDOT-PSS. However, achieving simultaneous improvements in efficiency, stability and reproducibility remains challenging. For example, carbazole-based SAMs exhibit low parasitic absorption and favourable hole selectivity, yet their poor energy-level alignment with Pb–Sn perovskites limits charge extraction[12,27,28]. Recent studies show that SAM molecules can be introduced directly into perovskite precursors, in which they self-assemble onto the substrate during film processing[29–31]. However, this approach may introduce competing interactions, as SAM molecules either anchor to the substrate or coordinate with the perovskite bulk, leading to insufficient hole transport and influenced crystallization dynamics of the perovskite formulation.

Moreover, the intrinsic self-p-doping of Pb–Sn perovskites, originating from Sn^{2+} oxidation and Sn vacancies[32], aggravates energy disorders by introducing surface traps that hinder charge extraction and exacerbate non-radiative recombination. These charge transport challenges become even more pronounced during large-area fabrication. Gas-assisted blade coating frequently results in non-uniform SAM coverage and triggers non-uniform crystallization in Pb–Sn perovskites[33–36]. The resulting lattice strain and defect formation degrade charge transport and device uniformity. Although molecular additives can modulate perovskite crystallization kinetics and partially relieve strain[37–39], their insulating nature compromises charge mobility. Therefore, achieving uniform Pb–Sn perovskite films with minimized defects, enhanced charge transport and stable interconnection remains an important requirement for scalable all-perovskite TSMs.

Here, we address these coupled challenges through a coordinated design of the TRJ and the perovskite interface. We introduce a fully solution-processed TRJ based on surface-engineered indium oxide nanocrystals (In_2O_3 NCs) with nanoscale morphology, whose energy levels and solvent compatibility can be systematically tuned through ligand chemistry. This NC-based junction combines high optical transparency with efficient carrier recombination while avoiding the absorption losses, instability and fabrication constraints associated with conventional metal-based TRJs. To ensure favourable band energy matching with the In_2O_3 NCs, we incorporate a phosphonic-acid-based HSM into the Pb–Sn perovskite precursor. This additive enhances hole transport and reduces defects by coordination, whereas its mediated crystallization control further enables scalable deposition by mitigating residual strain and sustaining uniform perovskite film quality across large areas. Through this synergistic interfacial and crystallization engineering strategy, we successfully fabricated all-perovskite TSMs with an aperture area of 65 cm^2, achieving a laboratory-measured PCE of 26.6% (independently certified at 26.2% by the Japan Electrical Safety and Environment Technology Laboratories, JET).

In_2O_3 NCs-based TRJ

Until now, all reported all-perovskite TSMs have used the conventional TRJ, typically composed of ALD-SnO_2/Au/PEDOT-PSS (referred to as 'type I' structure). Although this configuration enables high efficiencies in both tandem solar small cells and large modules, it has three intrinsic limitations: (1) metal (Au) diffusion at elevated temperatures; (2) the acidic degradation of PEDOT-PSS at the perovskite interface; and (3) strong parasitic absorption from the ultrathin Au and PEDOT-PSS layers. These intertwined optical and chemical instabilities suggest that gold-based TRJs have reached a fundamental ceiling for large-area perovskite tandems, motivating the development of a solution-processable and nonmetal interconnection with intrinsically uniform optical and electronic properties.

To address these inherent issues, we engineered two alternative recombination structures using solution process (Fig. 1a), a hole-transport-layer (HTL)-free TRJ from commercially available indium tin oxide (ITO NCs, type II) and an HTL-free TRJ based on self-synthesized In_2O_3 NCs (type III) (Supplementary Fig. 2). Electrical measurements of the three types of TRJ showed that the In_2O_3 NCs-based TRJ exhibited the desired ohmic contact behaviour, characterized by a linear *I*–*V* response that indicates the absence of a charge-transport barrier (Supplementary Fig. 3). Transmission electron microscopy (TEM) analysis shows that the self-synthesized In_2O_3 NCs are substantially smaller than commercial ITO NCs (Fig. 1b and Supplementary Fig. 4), enabling smoother interfaces with the perovskite layers and thus reducing contact defect density (Fig. 1c). Whereas type II provides a partially improved TRJ, type III uniquely combines nanoscale smoothness with optimized electronic contact, thereby motivating its use as the primary architecture in this study.

Optical characterization further shows the limitations of Type I TRJ. PEDOT-PSS introduces obvious parasitic absorption across 700–1,100 nm (Fig. 1d), directly impairing light harvesting in the Pb–Sn bottom subcell. Under thermal stress at 85 °C, these optical losses are accompanied by pronounced degradation (Fig. 1e). In particular, type I tandems retain <50% of their initial efficiency after only 50 h, whereas type II and type III architectures maintain about 75% of their initial performance after 200 h. Thus, NC-based TRJs simultaneously eliminate the two dominant loss channels, parasitic absorption and thermal instability, which fundamentally restrict Au/PEDOT-PSS junctions.

To directly probe the degradation pathways associated with PEDOT-PSS, we evaluated the thermal stability under 85 °C N_2 atmosphere on single-junction Pb–Sn perovskite solar cells (PSCs) using PEDOT-PSS, with an HTL-free device serving as the control. The PEDOT-PSS-based devices degraded to approximately 10% of their initial PCE within 150 h, whereas HTL-free devices maintained >15% efficiency after 400 h (Supplementary Fig. 5). These results confirm that the acidic, proton-rich PEDOT-PSS layer drives rapid interfacial decomposition in Pb–Sn perovskites, establishing it as a crucial reliability bottleneck at both the device and module levels.

The particular optical loss caused by the ultrathin gold layer presents a crucial, yet challenging, issue for maintaining uniformity during the upscaling of TSM fabrication. We systematically compared the optical absorption characteristics among thermally evaporated ultrathin Au layer, blade-coated ITO NC layer and blade-coated In_2O_3 NC layer on 10 × 10 cm^2 substrates (Fig. 1f). The ultrathin Au film exhibited substantial variation across eight measured points, whereas the blade-coated ITO and In_2O_3 NC layers maintained excellent homogeneity throughout the entire substrate area. This contrast highlights the superior scalability of solution-processed NC deposition compared with vacuum-evaporated ultrathin-layer techniques.

Building on the improved photon management achieved by In_2O_3 NC, we, therefore, prioritized the large-scale fabrication of perovskite films as an important preliminary step for developing all-perovskite TSMs. During the scale-up of Pb–Sn perovskite films, we identified that the reduced surface-to-volume ratio makes it particularly challenging to balance rapid solvent evaporation with required coating speeds during gas-assisted drying processes (Supplementary Fig. 6). Recognizing that the high boiling points and low evaporation rates of conventional solvents (dimethylformamide (DMF) and dimethyl sulfoxide (DMSO)) retard nucleation kinetics, we developed a binary cosolvent system with low boiling point and high evaporation rate of volatile coordinated 2-methoxyethanol (2-Me) and uncoordinated solvent of tetrahydrofuran (THF) to dissolve Pb–Sn perovskite precursors (Supplementary Fig. 7 and Supplementary Table 1). We found that the perovskite precursor can reach critical supersaturation with 20 vol% THF incorporation in Pb–Sn perovskite precursor for rapid nucleation and improved large-scale uniformity (Supplementary Fig. 8). The 2-Me-based Pb–Sn perovskite precursor enables high-speed blade coating at 30 mm s^{-1}, facilitated by its low boiling point and high vapour pressure. By contrast, the DMF-based system requires a slower coating speed of 5 mm s^{-1} for small-area devices (2.5 × 2.5 cm^2; Supplementary Fig. 9). This speed limitation becomes increasingly problematic during scale-up. Although the optimized coating speed must be progressively reduced for larger substrates, the DMF-based

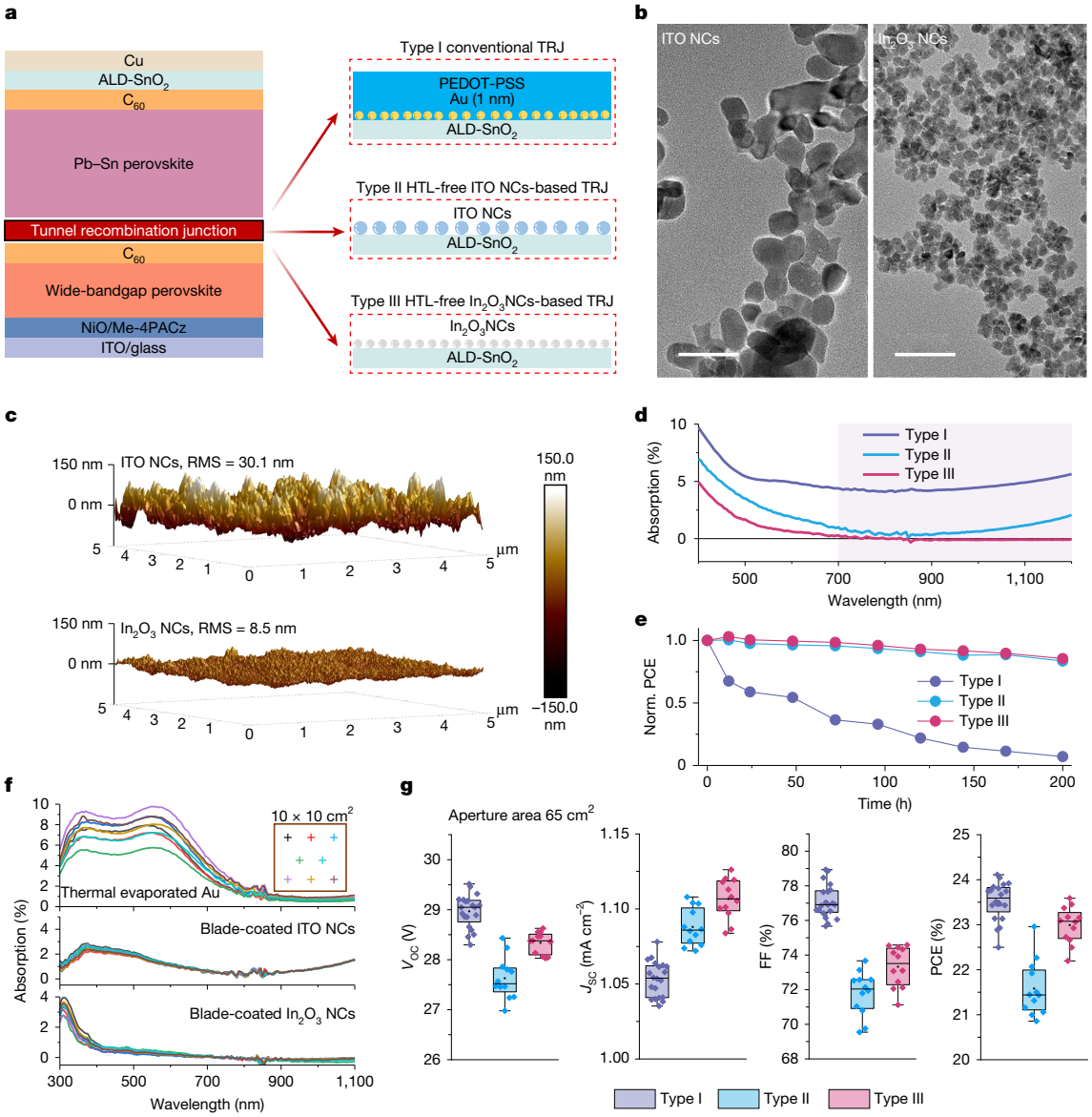

Fig. 1 | Tunnel recombination junctions in all-perovskite TSMs. a, Three types of TRJ in all-perovskite tandem structure. **b**, TEM images of ITO NCs and In_2O_3 NCs. **c**, Atomic force microscope images of ITO NCs and In_2O_3 NCs deposited on wide-bandgap subcells. **d**, Absorption of the three types of TRJ deposited on quartz. The coloured region is the response range of the Pb–Sn perovskite subcell in the tandem structure. **e**, Thermal stability of encapsulated all-perovskite TSMs using different TRJs under 85 °C ambient conditions. **f**, Optical absorption uniformity comparison among evaporated Au, blade-coated ITO NCs and blade-coated In_2O_3 NCs within 10 × 10 cm^2 substrates. **g**, Photovoltaic parameters of TSMs (aperture area 65 cm^2, 14 subcells in series) using three types of TRJ. Twenty devices were used for type I and 12 devices for types II and III. The boxes and whiskers represent the standard deviation and the maximum and minimum of the distributions, respectively. Scale bar, 50 nm (**b**, left and right). Me-4PACz, (4-(3,6-dimethyl-9-yl)butyl)phosphonic acid. RMS, root mean square roughness.

precursor fails to form uniform films even at 10 × 10 cm^2 scale, with complete crystallization failure occurring at 22 ×22 cm^2 dimensions. Then we characterized the uniformity of the perovskite films compared with DMF-based and 2-Me-based perovskite films deposited on 10 ×10 cm^2 substrates (Supplementary Fig. 10). Photoluminescence mapping showed significantly enhanced homogeneity and greater intensity uniformity in the 2-Me-based films compared with their DMF-based counterparts, directly correlating with improved device performance consistency across the substrate area (Supplementary Fig. 11). The incorporation of THF into the wide-bandgap perovskite can also improve coating speed and film uniformity, outperforming our previously reported green-solvent system (Supplementary Fig. 12). This improvement enabled a 17.5% efficiency on a 65 cm^2 aperture area (Supplementary Fig. 13), highlighting its excellent scalability of this approach.

Based on the improved scalability of perovskite films, the impact of these TRJ architectures was further evaluated in large-area all-perovskite TSMs. The module architecture consists of 14 series-connected subcells with individual widths of 5.75 mm, achieving a total aperture area of 65 cm^2 (Supplementary Fig. 14). The implementation of blade-coated NCs in TSMs significantly enhanced J_{SC} by eliminating parasitic absorption and non-uniformity. However, as shown in Fig. 1g, the removal of PEDOT-PSS introduced reduction in open-circuit voltage (V_{OC}) and fill factor (FF), attributable to increased non-radiative recombination and the formation of interfacial transport barriers between the perovskite layer and the ITO or In_2O_3 NC layers (Supplementary Fig. 15). These observations indicate that although NC-based TRJs successfully address the dominant optical and stability bottlenecks, their interfacial energetics require further optimization—particularly through surface tailoring of In_2O_3 NCs—to restore voltage and improve charge transport.

To verify that the superior performance of In_2O_3 NCs is intrinsic to the material rather than an artefact of thickness or morphological differences, we synthesized ITO NCs with comparable particle size using the same synthetic route (Supplementary Fig. 16). When deposited under identical conditions, the size-matched ITO NCs still exhibited inferior optical transparency and device performance compared with In_2O_3 NCs (Supplementary Fig. 17), confirming that the advantages of In_2O_3 NCs originate from their intrinsic material properties. To further quantify how these intrinsic advantages translate into scalable device performance, we performed optical and electrical simulations that account for key morphological factors. The simulations show that the In_2O_3 NC-based TRJ exhibits high tolerance to thickness variations and interfacial defects, which is important for maintaining performance uniformity across large-area modules (Supplementary Figs. 18 and 19).

Surface-tailoring of In_2O_3 NCs

To fully eliminate the residual interfacial barrier revealed after removing PEDOT-PSS, the NC-based TRJ must be further engineered to achieve precise energetic matching with the Pb–Sn perovskite. Conventional approaches that rely on carbazolyl derivatives or nickel oxide can partially mitigate interfacial band offsets[4,27]. But their effectiveness collapses under large-area processing, during which non-uniform molecular coverage and interfacial disorder generate spatially fluctuating barriers that suppress charge extraction (Supplementary Fig. 20). These limitations indicate that the energetics of the TRJ must be tuned intrinsically, which is through NC surface chemistry rather than by adding external hole-transport layers.

To address these challenges, we implemented a dual-level interfacial design (Fig. 2a): (1) tuning the work function of In_2O_3 NCs by surface ligand engineering to minimize the charge injection barrier at the perovskite/In_2O_3 NC interface; and (2) incorporating phosphonic-acid-based HSMs throughout the bulk of the Pb–Sn perovskite film, thereby enhancing bulk charge transport, rather than confining them solely to the interface.

To evaluate the efficiency of bulk HSM incorporation on charge transport, we constructed a series of HTL-free Pb–Sn PSCs as a diagnostic platform. In these devices, a library of phosphonic-acid-based HSMs was directly embedded within the perovskite matrix (Supplementary Fig. 21). As shown in Supplementary Fig. 22, all HSM candidates yielded PCEs exceeding 20%, with a consistent concentration of 0.2 mol%, revealing clear trends despite the potential for further performance enhancement through newly synthesized materials, various combinations and individual concentration optimization. However, we found that HSM is incompatible with the previously reported aminoacetamide hydrochloride (AAH) additive[2] (Supplementary Fig. 23). We attribute this mutual exclusivity to potential chemical interactions or competition between the amino-functionalized AAH and the phosphonic acid anchoring group of HSM at grain boundaries, which may disrupt passivation and charge extraction. This finding provides guidance for the selection and combination of additives in perovskite bulk. Notably, devices incorporating [2-(3,6-dimethoxy-9H-carbazol-9-yl)ethyl]phosphonic acid (MeO-2PACz), denoted as the representative 'target' films, achieved the highest performance, underscoring the influence of molecular design in optimizing charge extraction. This advantage arises from the electron-donating methoxy groups, which elevate the molecular energy levels and facilitate more efficient hole extraction, thereby enabling a better match with the energy level of the In_2O_3 NC layer[40] (Supplementary Fig. 24). Furthermore, incorporating HSM directly into the perovskite precursor proves more favourable for scalable fabrication than conventional monolayer coating, as achieving uniform and complete monolayer coverage over large areas remains challenging to control[41].

To investigate the charge-transport properties at the interface between In_2O_3 NCs and perovskite, we assessed their energy band alignment. The valence band maximum (VBM) is accurately determined by ionization energy from ultraviolet photoelectron spectroscopy (UPS) measurements performed under an applied negative bias voltage, as shown in Fig. 2b. The work function (Φ) was determined by Fermi edge obtained without an external bias voltage to avoid the influence of the electron acceleration potential on the highly conductive material (Fig. 2c and Supplementary Fig. 25). The resulting energy band alignment is shown in Fig. 2d. For the target perovskite film, the Φ increased to 4.81 eV and the VBM shifted to 5.31 eV, compared with 5.04 eV and 5.70 eV for the control film, respectively. These shifts concurrently indicate that the target film exhibits a reduced n-type character relative to the control.

Oleylamine (OAm)-capped In_2O_3 NCs were synthesized according to a previously published procedure[42]. We found that ligand engineering could effectively tune the work function of these NCs. The choice of ligands was guided by a stepwise ligand-engineering strategy rather than empirical screening, aiming to achieve stable surface anchoring, compatibility with green-solvent processing, and tunable interfacial energy-level alignment while preserving the NC structure (Supplementary Note 2). To this end, ligand exchange was performed using mono-2-(methacryloyloxy)ethyl succinate (MMES) and 5-(4-(methacryloyloxy)–3-methoxyphenyl)pent-4-enoic acid (MMPA) (Supplementary Fig. 26). As the Fermi level must be flat across the heterojunction at equilibrium, band bending near an interface determinate the charge transport at the interface between the perovskite bulk and In_2O_3 NCs. The reasonable energy band alignment is shown in Supplementary Fig. 27; the energy band of target perovskite film shifted upwards by 50 meV near the interface with In_2O_3-MMPA NCs, which is beneficial for hole transport. Conversely, OAm- and MMES-capped In_2O_3 NCs induce a downward band bending at the interface, creating a notable charge-transport barrier. To exclude the influence of the ligands on charge transport, we further characterized the interfacial defects and hole mobility using space-charge-limited current measurements (Supplementary Figs. 28 and 29). The results show negligible differences in trap density and mobility between MMES- and MMPA-capped In_2O_3, confirming that the enhanced hole extraction primarily originates from the optimized energy band alignment rather than altered transport properties.

To explain the mechanism of the charge transport in HSM-incorporated perovskite, we calculated the differential lifetime by analysing the fitted time-resolved photoluminescence of perovskite films deposited on In_2O_3-MMPA NCs, measured from the substrate side (Supplementary Fig. 30). The sharp increase of differential lifetime in early time could be attributed to the charge extraction at interface. To further investigate the hole transport of Pb–Sn perovskite bulk, we systematically reduce the thickness of PEDOT-PSS from 24 nm to complete removal, which revealed a pronounced performance enhancement in target devices compared with controls (Fig. 2e). The average J_{SC} showed a consistent increase as PEDOT-PSS thickness decreased, reaching optimal values in its complete absence, which we attribute to minimized parasitic absorption and enhanced hole transport (Supplementary Fig. 31). We optimized the concentration of the MeO-2PACz at 0.2 mol% to obtain a champion performance based on the HTL-free device (Supplementary Fig. 32). For the best-performing HTL-free device, it demonstrates a high efficiency of 23%, with significantly improved J_{SC} of 33.6 mA cm^{-2} (Supplementary Fig. 33). The improved performance of the HTL-free device can be attributed to the enhanced hole transport within the perovskite film.

To validate the enhanced hole-transport properties of In_2O_3 NCs in a tandem structure, we fabricated blade-coated Pb–Sn PSCs using target perovskite films with different In_2O_3 NCs as HTLs (Fig. 2f). Although devices with In_2O_3-OAm and In_2O_3-MMES NCs maintained a relatively high FF due to self-p-doping, the champion device based on In_2O_3-MMPA NCs achieved a remarkable reverse-scan PCE of 24.0%, with a J_{SC} of 33.8 mA cm^{-2}, a V_{OC} of 0.859 V and an FF of 82.6%. The corresponding external quantum efficiency (EQE) spectra are shown in Fig. 2g. The integrated J_{SC} from the EQE spectrum of the In_2O_3-MMPA

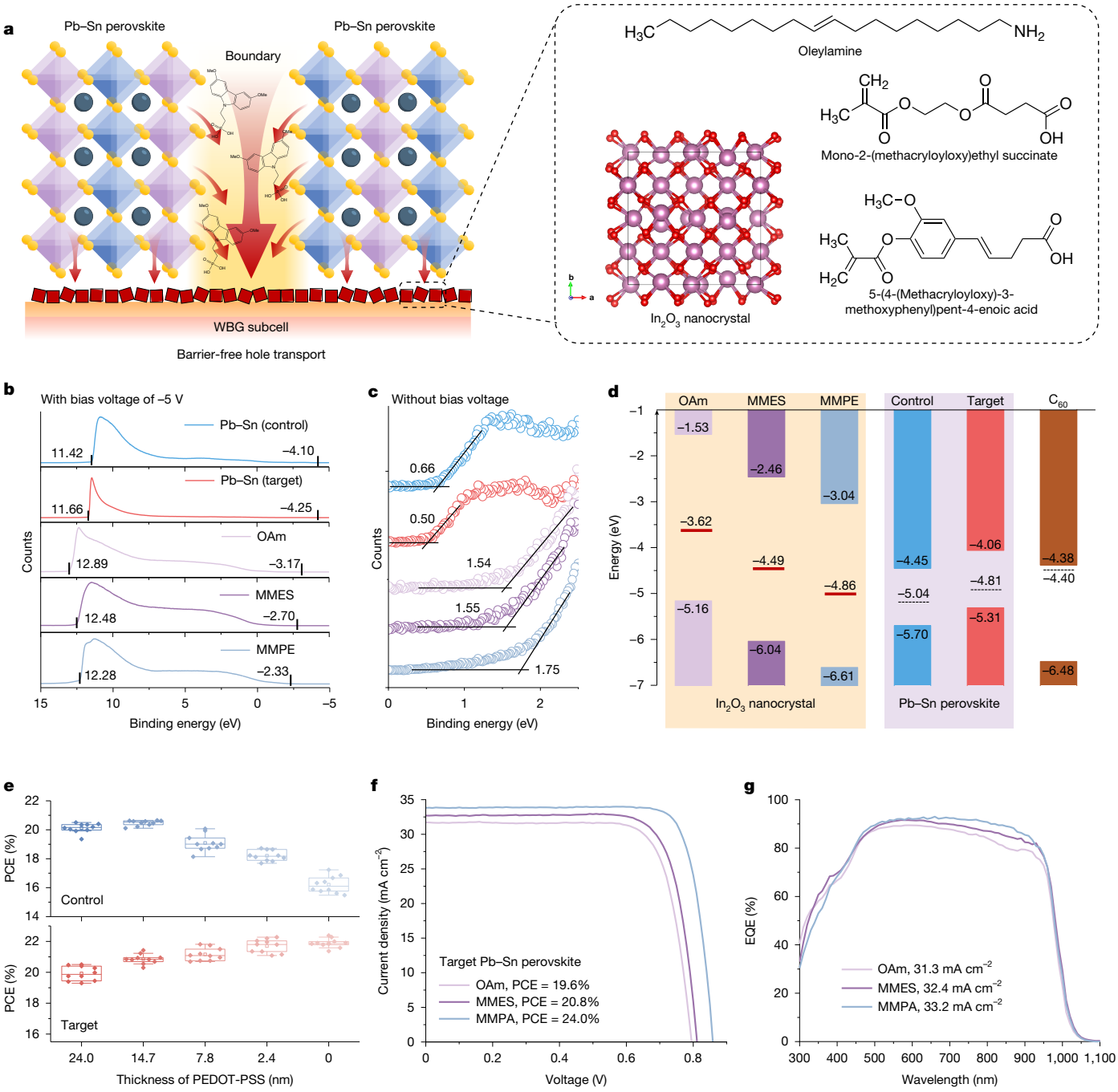

Fig. 2 | Enhanced charge transport in Pb–Sn PSCs. a, Schematic of the co-optimization strategy: incorporating HSMs into the perovskite bulk and engineering the surface ligands of In_2O_3 NCs. **b**, UPS spectra of the control and target perovskite films, as well as In_2O_3 NCs with different surface ligands, measured under an applied bias voltage. **c**, Close-up of the Fermi edge region from the UPS spectra of the samples measured without an external bias voltage. **d**, Energy-level alignment diagram for the various In_2O_3 NCs, perovskite films and C_{60} derived from the UPS results. **e**, Photovoltaic performance of control and target Pb–Sn PSCs fabricated with reduced PEDOT-PSS thicknesses. Ten devices were used for each type with aperture area of 0.049 cm^2. The boxes and whiskers represent the standard deviation and the maximum and minimum of the distributions, respectively. **f**, *J*–*V* curves of the champion target PSCs based on In_2O_3 NCs with different ligands (aperture area 0.049 cm^2). **g**, EQE curves of the corresponding best-performing PSCs shown in **f**. WBG, wide bandgap.

device (33.2 mA cm^{-2}) significantly exceeds that of the In_2O_3-OAm (31.3 mA cm^{-2})-based and In_2O_3-MMES (32.4 mA cm^{-2})-based devices, corroborating the enhanced hole transport.

HSM-modulated Pb–Sn perovskites

Beyond enhancing charge transport through its incorporation into Pb–Sn perovskites, the HSM additive is believed to have other profound functions that warrant further exploration. To investigate the film crystallization and carrier dynamic, we first characterized the perovskite film morphology among top, bottom and cross-sectional sides by scanning electron microscopy (SEM) (Supplementary Fig. 34). The control sample shows distinct grain boundaries, accompanied by branched impurities existing in the whole bulk. As the HSMs incorporated, the target sample demonstrates disappeared impurities and enlarged grain domains, which seem melted boundaries among micrograins (Supplementary Fig. 35). We noticed that all the phosphonic-acid-based HSMs can distribute and fill the domain boundaries, as well as suppressing

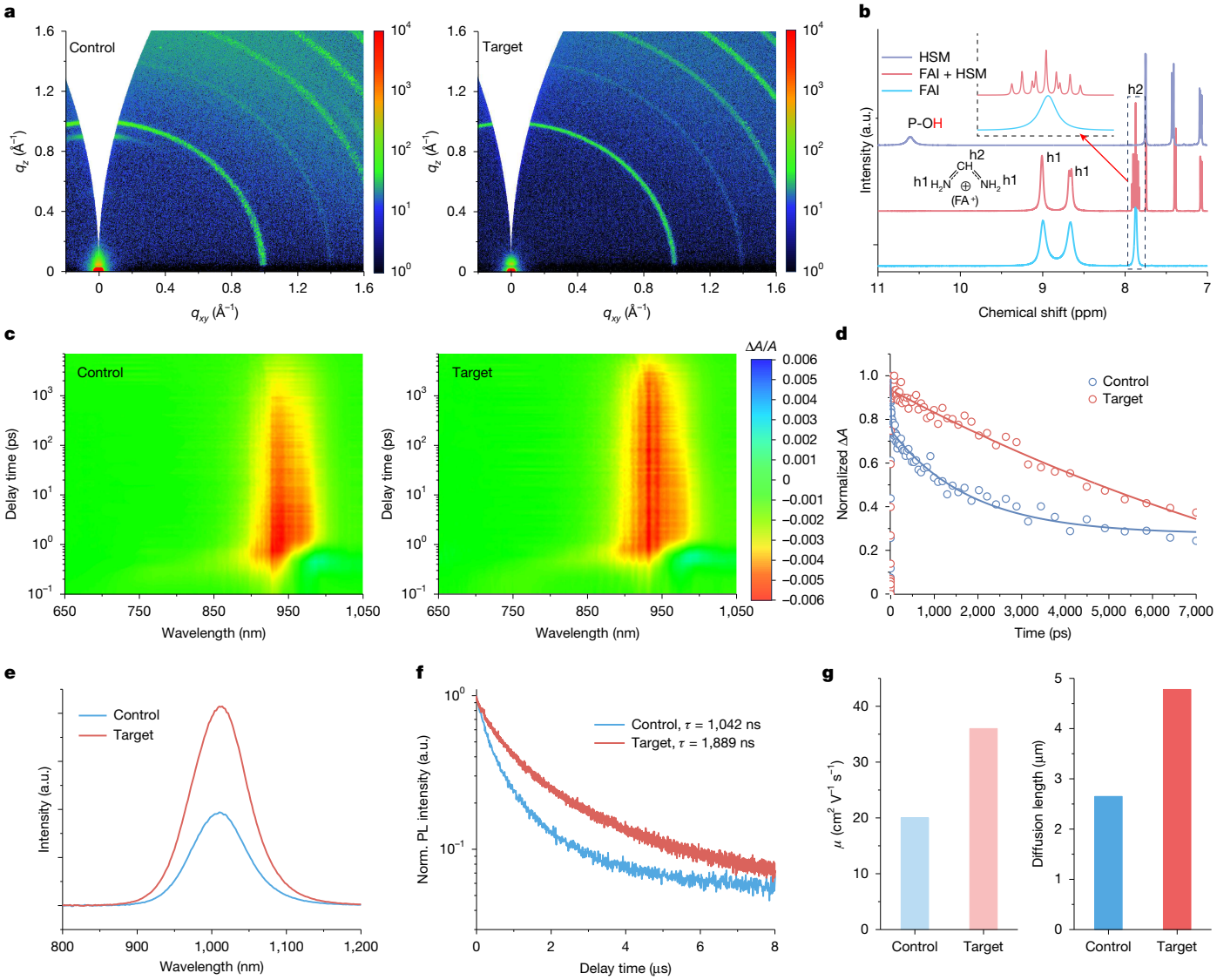

Fig. 3 | Characteristics of Pb–Sn perovskite films. a, GIWAXS patterns of control and target Pb–Sn perovskite films. **b**, ^{1}H nuclear magnetic resonance spectra of HSM, FAI and HSM + FAI mixture in DMSO-d_6 solution. The H corresponding to the position is marked in red. **c**, TAS study of the control and target Pb–Sn perovskite film deposited on quartz. **d**, Carrier decay of control and target Pb–Sn perovskite films from transient absorption. **e**,**f**, Steady-state (**e**) and time-resolved photoluminescence (**f**) spectra of control and target Pb–Sn perovskite films deposited on quartz. **g**, Mobilities and diffusion lengths of the control and target Pb–Sn perovskite films. a.u., arbitrary units.

the formation of impurities (Supplementary Fig. 36). Beyond the type of HSM used, we observed that Pb–Sn perovskite films fabricated using the DMF-based solvent system also exhibited the similar morphology (Supplementary Fig. 37). To reveal the formation of the impurities and melted boundaries, we studied the crystallization of perovskite. We observed that the incorporation of HSMs can suppress the formation of PbI_2 (Supplementary Fig. 38), as confirmed by grazing-incidence wide-angle X-ray scattering (GIWAXS) analysis (Fig. 3a). The natural deprotonation of FA^+ cations leads to A-site vacancies and unreacted PbI_2 accumulation[43]. Liquid-phase ^{1}H NMR spectroscopy (Fig. 3b) shows the role of HSM in mitigating this issue. On mixing HSM with FAI, the proton signal corresponding to the phosphonic acid group (P–OH) disappears completely, indicating deprotonation of the phosphonic acid functionality in the precursor solution. Concurrently, the FA^+ proton resonance evolves from a broad peak into a resolved multiplet with only a minor chemical-shift change. This spectral evolution suggests the presence of weak interactions between the deprotonated HSM species and FA^+ in solution. These interactions perturb the local environment of the FA^+ ammonium protons and may partially break the symmetry of the FA^+ cation, giving rise to the observed multiplet structure. The minimal shift in resonance indicates that the interaction remains relatively weak, consistent with a dynamic solution-phase association rather than the formation of a strongly bound complex. The preferential deprotonation of HSM consumes free acidic phosphonic acid groups that would otherwise directly acidify FA^+ and induce its detrimental deprotonation. Instead, through these weak interactions, HSM effectively suppresses the deprotonation of FA^+, thereby stabilizing the chemical environment of the precursor solution[7].

We next performed ultrafast transient absorption spectroscopy (TAS) to investigate the charge dynamics resulting from the incorporation of HSMs in the perovskite film, which was deposited on a quartz substrate. We observed that the photo-bleaching peaks around 930 nm remained consistent without any noticeable shift for both the control and target samples (Fig. 3c), indicating a substantially spatially uniform phase in the Pb–Sn perovskite films. The decay kinetics were analysed in Fig. 3d. The fast decay process is probably associated with non-radiative recombination of electrons and holes through defects in the perovskite film. By contrast, the slower decay process observed

in the target film can be attributed to the radiative recombination of free electrons and holes within the perovskite film, resulting from the suppression of impurity in perovskite films.

We then observed that the target film exhibited obviously stronger steady-state photoluminescence emission compared with the control film (Fig. 3e). The average photoluminescence decay lifetime (τ) of the target film calculated is 1,889 ns, which is longer than that of the control film (τ = 1042 ns) (Fig. 3f and Supplementary Table 1). We further investigated the top and bottom surfaces of the perovskite films, observing that the bottom surface of the target film exhibited enhanced photoluminescence intensity (Supplementary Fig. 39). This finding suggests that the HSMs can effectively passivate both sides of the film, especially reducing charge trapping at buried boundaries. However, on removal of the target perovskite film, we noticed no residual HSMs on the ITO substrates (Supplementary Fig. 40). This observation suggests that, when incorporated into the perovskite precursor solution throughout the film formation process, HSMs exhibit a preferential affinity for perovskites over the ITO substrate. Consequently, the phosphonic acid anchoring group appears to preferentially associate with perovskite grains rather than the ITO substrate, highlighting the selective and robust nature of the HSM–perovskite interaction. To verify this, the shifted Fourier-transform infrared spectroscopy peak of P = O bond (Supplementary Fig. 41) and the strengthened binding energy of Pb 4*f* and Sn 3*d* confirm the interaction between HSMs and perovskites (Supplementary Fig. 42). We considered that the HSMs with the lone-pair electrons in the O-donor of P = O bond can coordinate with the octahedral framework (for example, $[PbI_6]^{4-}$, $[SnI_6]^{4-}$) by dative bonding at the boundaries. The phosphonic acid anchor in the HSM also acts as an antioxidant barrier, substantially suppressing oxidation in the Pb–Sn perovskite. This protection is crucial for maintaining material integrity during transient air exposure, such as in the P2/P3 scribing steps or module measurement, which is essential for practical processing and operation (Supplementary Fig. 43).

We then performed femtosecond-resolved optical-pump terahertz-probe spectroscopy to obtain the carrier mobility and diffusion length of perovskite films. Supplementary Fig. 44 shows the transient THz transmission dynamics for control and target thin films (about 1,100 nm thickness) under varying pump fluences. The recombination rate constants and charge-carrier mobilities for control and target samples were calculated as 20 and 36 $cm^2 V^{-1} s^{-1}$, respectively (for details, see Supplementary Note 3 and Supplementary Fig. 45). Owing to the longer carrier lifetimes, the diffusion length of the target film increased to 4.78 µm compared with 2.65 µm for the control film (Fig. 3g). These findings indicated that the target film exhibits improved film quality and suppressed non-radiative recombination channels.

All-perovskite TSMs

Although we achieved a compact and macroscopically uniform Pb–Sn perovskite film on the 10 × 10 cm^2 substrates, the processing window in coating time caused asynchronous nucleation, which in turn led to microscopic morphological differences[2]. This results in excessive nucleation at the beginning of blade coating, which leads to grain extrusion and subsequently compressive strain in the perovskite films[35,36]. As shown in Fig. 4a, we compared four points along the coating direction of the Pb–Sn perovskite film. The target film showed consistent surface morphology across all points, unlike the control film, which exhibited grain compression at the start of the blade coating path. Our lattice stress analysis revealed a notable shift in the (100) diffraction peak towards higher angles in perovskite films compared with strain-free scraped powder (Fig. 4b). This observation demonstrates that the rapid, concentrated crystallization process in large-scale control films induces compressive strain. By contrast, the target films incorporating HSMs at grain boundaries effectively alleviate this lattice stress, as evidenced by the reduced peak shift. Then we fabricated the In_2O_3-MMPA NCs-based Pb–Sn perovskite solar modules with an aperture area of 65 cm^2 using 2-Me-based perovskite ink with HSM incorporation (Supplementary Fig. 46). The champion Pb–Sn perovskite solar module exhibits significantly enhanced J_{SC} and FF, thus achieving a remarkable efficiency of 19.9%, which surpasses the 13.8% of the control module (Fig. 4c and Supplementary Table 3).

Building on the superior charge-transport properties and enhanced uniformity achieved in HSM-incorporated Pb–Sn perovskite films, we developed large-area all-perovskite TSMs implementing type-III-based TRJ (Supplementary Fig. 47), benchmarking against the conventional type-I architecture. Notably, the TSM with type-III TRJ exhibited significantly higher J_{SC} values and FF (Supplementary Fig. 48), which we primarily attribute to two key factors: (1) reduced parasitic absorption losses and (2) enhanced interfacial charge transport.

The best-performing TSM with type-I TRJ exhibited a PCE of 24.9% under the reverse scan, with a V_{OC} of 29.3 V, a J_{SC} of 1.09 mA cm^{-2} and an FF of 77.8% (Fig. 4d and Supplementary Table 4). The champion TSM with type-III TRJ exhibited a high PCE of 26.6% under both reverse and forward scans, with a V_{OC} of 30.4 V, a J_{SC} of 1.12 mA cm^{-2} and an FF of 78.2%. The TSM showed a steady-state PCE of 26.5% at the maximum power point (MPP) voltage of 25.6 V measured for 5 min (Supplementary Fig. 49). We achieved certified stabilized PCEs of 24.8% and 26.2% for the two types of TSMs, as measured by JET[5,44] (Supplementary Fig. 50). Considering a high geometric FF of 96.5%, which we optimized the death area to 200 µm (Supplementary Note 4 and Supplementary Figs. 51–54), the active-area efficiency of the TSM reached 27.6%. This work represents a dual breakthrough in both efficiency and device area in all-perovskite TSM development, surpassing all existing performance benchmarks in the field (Supplementary Fig. 55).

To understand the improvement of J_{SC}, we characterized EQEs of 16 distinct locations across the TSM (Supplementary Fig. 51). As shown in Fig. 4e, the average integrated J_{SC} values of these 16 points obtained from EQE spectra for both top and bottom subcells are 16.3 mA cm^{-2} and 16.2 mA cm^{-2}, respectively, in good agreement with the J_{SC} determined from *J*–*V* measurements. The J_{SC} of the TSM surpasses that of reported TSMs, which show low current density per subcell below 15 mA cm^{-2} (Supplementary Table 5).

To evaluate the reliability superiority of the type-III TRJ in our TSM, we conducted accelerated stability tests adhering to the International Electrotechnical Commission (IEC) 61215:2021 standard for terrestrial photovoltaic modules, with direct comparison to a conventional type-I TRJ[45]. The operational stability of an encapsulated TSM was tracked under simulated 1-sun illumination in ambient air (Fig. 4f). The module using the type-III TRJ retained 90% of its initial PCE (T90, initial PCE = 24.6%; Supplementary Fig. 56) after 771 h and 82.5% (T82.5) after 1,000 h. Our analysis indicates that the significant performance degradation of the TSM is primarily attributable to the type-I TRJ, which induces the degradation of the Pb–Sn perovskite film (Supplementary Fig. 57).

To assess performance under extreme conditions, we subjected devices to continuous illumination at open circuit on a 65 °C hotplate (ISOS-L-3 protocol; Supplementary Fig. 58). The type-III TRJ module demonstrated exceptional stability throughout the 120-h test. Furthermore, under damp-heat testing (85 °C and 85% relative humidity, ISOS-D-3; Supplementary Fig. 59), the encapsulated type-III TRJ modules exhibited an average T84 lifetime of 1,000 h, compared with a retention of below 40% for the type-I TRJ modules. We attribute the pronounced degradation of the type-I modules primarily to the thermal instability of the PEDOT-PSS layer, which is consistent with the thermal degradation trend observed in Fig. 1e. By contrast, the more gradual degradation of the type-III modules is mainly limited by the intrinsic instability of the MAFA perovskite composition, which is known to be less robust than MA-free or all-FA analogues. Finally, when subjected to thermal cycling between −40 °C and 85 °C (ISOS-T-3, Supplementary Fig. 60), these modules retained 93% of their initial PCE after 200 cycles, demonstrating superior stability compared with our previous work.

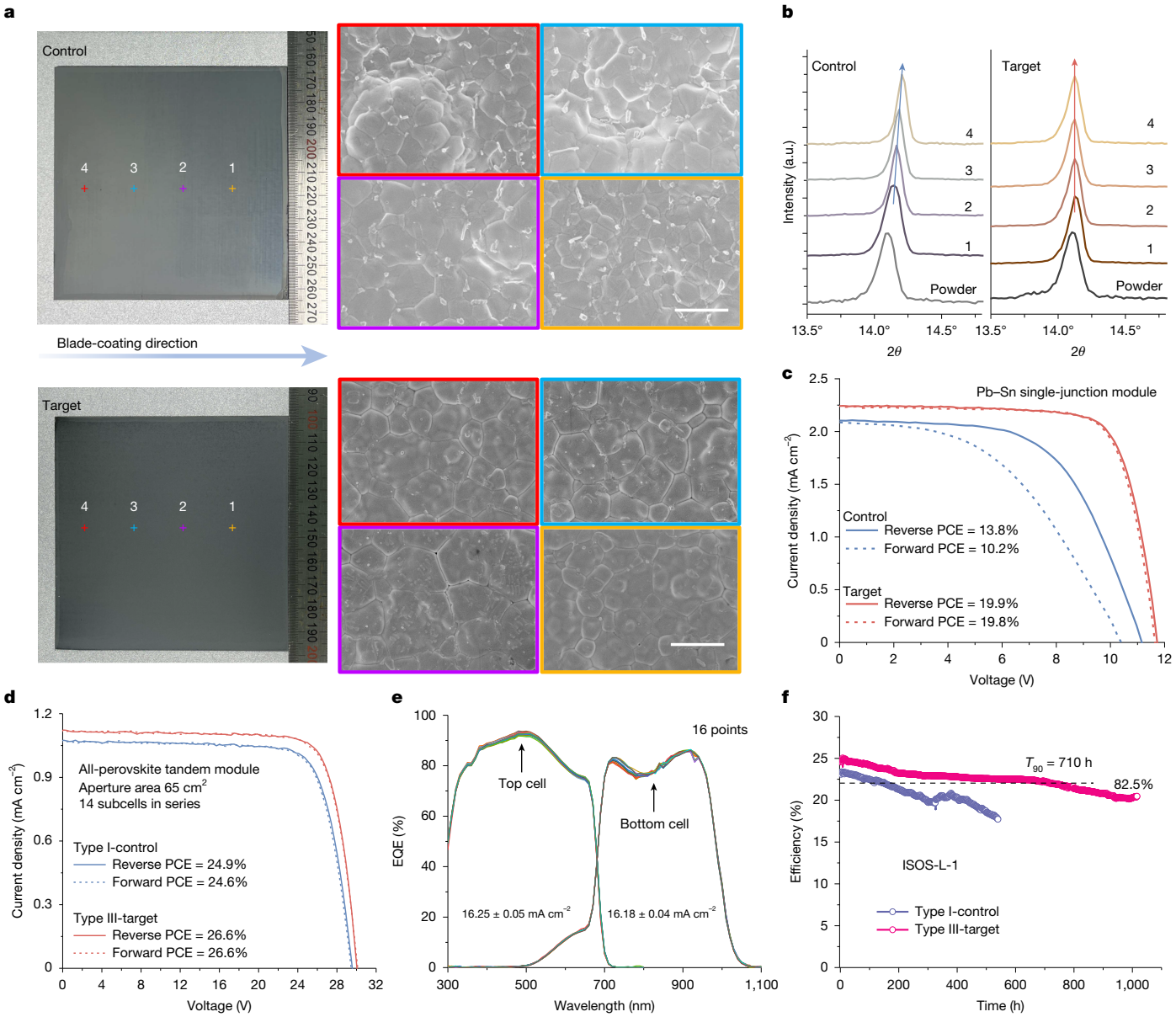

Fig. 4 | Large-scale fabrication of Pb–Sn perovskite films and all-perovskite TSMs. a, Digital photos and SEM images of control and target Pb–Sn perovskite films. **b**, XRD patterns of control and target Pb–Sn perovskite films. **c**, *J*–*V* curves of the best-performing control and target Pb–Sn perovskite solar modules. The aperture area is 65 cm^2 with 14 subcells in series. **d**, *J*–*V* curves of the best-performing TSMs using type I and type III TRJs. **e**, EQE spectra statistics from 16 points in the corresponding champion TSM. **f**, PCE evolution of the encapsulated modules measured at MPP under continuous 1-sun illumination in ambient air and at room temperature. a.u., arbitrary units. Scale bar, 2 μm (**a**). ISOS, International Summit on Organic Photovoltaic Stability.

In conclusion, this work demonstrates a 26.2% efficient all-perovskite tandem solar module with an aperture area of 65 cm^2, achieved through an NC-based recombination layer that simultaneously addresses both scaling- and stack-driven limitations. The In_2O_3 NC layer mitigates stack-driven parasitic absorption and instability inherent to conventional architectures. Furthermore, its thickness-insensitive optoelectronic properties and favourable interfacial characteristics, combined with the uniform crystallization of Pb–Sn perovskite films achieved by HSM incorporation, effectively overcome key challenges associated with module scaling. The concurrent improvements in module size, efficiency and operational stability underscore the strong commercialization potential of all-perovskite tandem photovoltaics, positioning them as a viable competitor to conventional silicon photovoltaics. To further advance this technology towards practical application, scaling the module area beyond 800 cm^2 will require synergistic developments in both deposition and crystallization processes. Specifically, advancements in slot-die coating techniques must be coupled with optimized crystallization methods, such as vacuum-assisted crystallization, to ensure the high-quality and uniform fabrication of both wide-bandgap and narrow-bandgap perovskite subcells over large areas.

Online content

Any methods, additional references, Nature Portfolio reporting summaries, source data, extended data, supplementary information, acknowledgements, peer review information; details of author contributions and competing interests; and statements of data and code availability are available at https://doi.org/10.1038/s41586-026-10768-1.

1. Xiao, K. et al. Scalable processing for realizing 21.7%-efficient all-perovskite tandem solar modules. *Science* **376**, 762–767 (2022).
2. Gao, H. et al. Homogeneous crystallization and buried interface passivation for perovskite tandem solar modules. *Science* **383**, 855–859 (2024).

3. Liu, C., Gao, H., Ou, W., Tan, H. & Lin, R. Light management in monolithic all-perovskite tandem solar cells. *Light Sci. Appl.* **15**, 56 (2026).
4. Gao, H. et al. Thermally stable all-perovskite tandem solar cells fully using metal oxide charge transport layers and tunnel junction. *Sol. RRL* **5**, 2100814 (2021).
5. Green, M. A. et al. Solar cell efficiency tables (version 66). *Prog. Photovolt. Res. Appl.* **33**, 795–810 (2025).
6. Xiao, K. et al. All-perovskite tandem solar cells with 24.2% certified efficiency and area over 1 cm^2 using surface-anchoring zwitterionic antioxidant. *Nat. Energy* **5**, 870–880 (2020).
7. Duan, C. et al. Scalable fabrication of wide-bandgap perovskites using green solvents for tandem solar cells. *Nat. Energy* **10**, 318–328 (2024).
8. Lin, R. et al. All-perovskite tandem solar cells with dipolar passivation. *Nature* **648**, 600–606 (2025).
9. Lin, R. et al. All-perovskite tandem solar cells with 3D/3D bilayer perovskite heterojunction. *Nature* **620**, 994–1000 (2023).
10. Liu, Z. et al. All-perovskite tandem solar cells achieving >29% efficiency with improved (100) orientation in wide-bandgap perovskites. *Nat. Mater.* **24**, 252–259 (2025).
11. Kim, H. et al. Highly efficient hole transport layer-free low bandgap mixed Pb–Sn perovskite solar cells enabled by a binary additive system. *Adv. Funct. Mater.* **32**, 2110069 (2022).
12. Kapil, G. et al. Tin-lead perovskite solar cells fabricated on hole selective monolayers. *ACS Energy Lett.* **7**, 966–974 (2022).
13. Wen, J. et al. Present status of and future opportunities for all-perovskite tandem photovoltaics. *Nat. Energy* **10**, 681–696 (2025).
14. Lin, R. et al. All-perovskite tandem solar cells with improved grain surface passivation. *Nature* **603**, 73–78 (2022).
15. Wang, Y. et al. Homogenized contact in all-perovskite tandems using tailored 2D perovskite. *Nature* **635**, 867–873 (2024).
16. Pan, H. et al. Decoupling photothermal-mechanical degradation through lattice-stabilizing networks in Sn–Pb perovskites and all-perovskite tandem solar cells. *Nat. Commun.* **16**, 9221 (2025).
17. Hu, S. et al. Optimized carrier extraction at interfaces for 23.6% efficient tin–lead perovskite solar cells. *Energy Environ. Sci.* **15**, 2096–2107 (2022).
18. Chin, Y.-C., Daboczi, M., Henderson, C., Luke, J. & Kim, J.-S. Suppressing PEDOT:PSS doping-induced interfacial recombination loss in perovskite solar cells. *ACS Energy Lett.* **7**, 560–568 (2022).
19. Yu, Z. et al. Simplified interconnection structure based on C_{60}/SnO_{2-x} for all-perovskite tandem solar cells. *Nat. Energy* **5**, 657–665 (2020).
20. Han, Q. et al. Low-temperature processed inorganic hole transport layer for efficient and stable mixed Pb-Sn low-bandgap perovskite solar cells. *Sci. Bull.* **64**, 1399–1401 (2019).
21. Zhou, Y. et al. Defect-less formamidinium Sn-Pb perovskite grown on a fluorinated substrate with top-down crystallization control for efficient and stable photovoltaics. *Energy Environ. Sci.* **17**, 2845–2855 (2024).
22. Zhou, Y. et al. Manipulation of the buried interface for robust formamidinium-based Sn–Pb perovskite solar cells with NiO_x hole-transport layers. *Angew. Chem.* **135**, e202300759 (2023).
23. Zhu, J. et al. A donor–acceptor-type hole-selective contact reducing non-radiative recombination losses in both subcells towards efficient all-perovskite tandems. *Nat. Energy* **8**, 714–724 (2023).
24. Xu, G. et al. Integrating ultrathin bulk-heterojunction organic semiconductor intermediary for high-performance low-bandgap perovskite solar cells with low energy loss. *Adv. Funct. Mater.* **28**, 1804427 (2018).
25. Ma, T. et al. Hole transport layer-free low-bandgap perovskite solar cells for efficient all-perovskite tandems. *Adv. Mater.* **36**, e2308240 (2024).
26. You, J. et al. Eco-friendly glucose assisted structurally simplified high-efficiency tin-lead mixed perovskite solar cells. *J. Energy Chem.* **85**, 83–90 (2023).
27. Liu, C. et al. Efficient all-perovskite tandem solar cells with low-optical-loss carbazolyl interconnecting layers. *Angew. Chem. Int. Ed.* **62**, e202313374 (2023).
28. Zhang, Z. et al. Anchoring charge selective self-assembled monolayers for tin–lead perovskite solar cells. *Adv. Mater.* **36**, e2312264 (2024).
29. Dai, Z. et al. Synergistic regulation of defects, charge carriers, and ions via bimolecular engineering in carbon-based perovskite photovoltaics. *Joule* **10**, 102298 (2026).
30. Tan, Q. et al. Inverted perovskite solar cells using dimethylacridine-based dopants. *Nature* **620**, 545–551 (2023).
31. Zheng, X. et al. Co-deposition of hole-selective contact and absorber for improving the processability of perovskite solar cells. *Nat. Energy* **8**, 462–472 (2023).
32. Sun, Q. et al. Surface charge transfer doping of narrow-bandgap Sn–Pb perovskites for high-performance tandem solar cells. *Energy Environ. Sci.* **17**, 2512–2520 (2024).
33. Park, S. M. et al. Low-loss contacts on textured substrates for inverted perovskite solar cells. *Nature* **624**, 289–294 (2023).
34. Liu, S. et al. Buried interface molecular hybrid for inverted perovskite solar cells. *Nature* **632**, 536–542 (2024).
35. Zhang, H. & Park, N.-G. Strain control to stabilize perovskite solar cells. *Angew. Chem. Int. Ed.* **61**, e202212268 (2022).
36. Kang, Y. et al. Thermal shock fabrication of ion-stabilized perovskite and solar cells. *Adv. Mater.* **34**, 2203166 (2022).
37. Chen, C.-H. et al. Full-dimensional grain boundary stress release for flexible perovskite indoor photovoltaics. *Adv. Mater.* **34**, 2200320 (2022).
38. Chen, Z. et al. Perovskite grain-boundary manipulation using room-temperature dynamic self-healing "ligaments" for developing highly stable flexible perovskite solar cells with 23.8% efficiency. *Adv. Mater.* **35**, 2300513 (2023).
39. Liu, W. et al. Defect engineering and crystallization kinetics control via dual-functional mercaptoacetamide for high-performance, large-area perovskite solar modules. *Adv. Mater.* **15**, e02193 (2025).
40. Chen, C.-H. et al. Methylthio substituent in SAM constructing regulatory bridge with photovoltaic perovskites. *Angew. Chem. Int. Ed.* **64**, e202419375 (2025).
41. Pradhan, S. et al. Interfacial dipole engineering via boronic acid-based self-assembled monolayers in inverted tin–lead perovskite solar cells with ideal band gap. *ACS Energy Lett.* **10**, 4983–4994 (2025).
42. Lounis, S. D., Runnerstrom, E. L., Bergerud, A., Nordlund, D. & Milliron, D. J. Influence of dopant distribution on the plasmonic properties of indium tin oxide nanocrystals. *J. Am. Chem. Soc.* **136**, 7110–7116 (2014).
43. Zhu, J. et al. All-in-one Lewis base for enhanced precursor and device stability in highly efficient perovskite solar cells. *ACS Energy Lett.* **6**, 3425–3434 (2021).
44. Green, M. A. et al. Solar cell efficiency tables (version 65). *Prog. Photovolt. Res. Appl.* **33**, 3–15 (2025).
45. Khenkin, M. V. et al. Consensus statement for stability assessment and reporting for perovskite photovoltaics based on ISOS procedures. *Nat. Energy* **5**, 35–49 (2020).

Methods

Materials

All materials were used as received without further purification. The organic halide salts (FAI, MAI, FABr and phenylethylammonium iodide with purity of >99%) were purchased from GreatCell Solar Materials. PEDOT-PSS aqueous solution (Al 4083) was purchased from Heraeus Clevios. All the hole-selective materials and PbX_2 (X = I/Br) (99.99%, trace metals basis) were purchased from TCI. SnI_2 (99.999%, trace metals basis) was purchased from Alfa Aesar. SnF_2 (99%), tin powders (<150 μm, 99.5%), CsI (99.9%), CsBr (99.9%), 2-methoxyethanol (99.8% anhydrous), THF (99.9% anhydrous, inhibitor-free), DMF (99.8% anhydrous), DMSO (99.9% anhydrous) and ITO NCs solution (30 wt% in IPA) were purchased from Sigma-Aldrich. C_{60} was purchased from Nano-C. Indium acetate ($In(ac)_3$, 99.99%) was purchased from Meryer Technologies. Octanoic acid (OctAC, 99%), mono-2 (methacryloyloxy) ethyl succinate (MMES, >95%), propylene glycol monomethyl ether acetate (PGMEA, >99.5%) and octyl ether (99%) were purchased from Aldrich. Oleylamine (OLAM, 90%) was purchased from Acros. Vanillin (98%) was purchased from Energy Chemical. 3-Carboxyprop-1-yltriphenylphosphonium bromide (97%) was purchased from Amethyst. Methacryloyl chloride (99%) and lithium bis(trimethylsilyl)amide (Li-HMDS, 1.0 M solution in THF) were purchased from J&K. It should be noted that THF is a hazardous solvent that can form explosive peroxides, and it should only be handled by trained personnel using appropriate safety protocols, including regular peroxide testing, storage under inert conditions and avoidance of evaporation to dryness.

Synthesis of MMPA

A 5 mmol portion of 3-carboxyprop-1-yl triphenylphosphonium bromide was dissolved in anhydrous THF, and 11 ml of 1.0 M lithium hexamethyldisilazide in THF was added dropwise in an ice bath (0 °C). After stirring for 2 h, a THF solution of vanillin (5 mmol) was added slowly, and the mixture was stirred overnight at room temperature. The reaction was quenched with water and acidified to pH <2 with dilute H_2SO_4. The mixture was extracted with ethyl acetate (EtOAc), the combined organic layers were washed with water and dried over anhydrous Na_2SO_4, and the crude material was purified by column chromatography (30% v/v EtOAc in hexane) to give the intermediate. The intermediate was dissolved in an aqueous NaOH solution (2.2 equiv.), and methacryloyl chloride (2.0 equiv) was added dropwise in an ice bath. After stirring at room temperature for 2 h, the mixture was acidified with HCl to pH <2 and extracted with EtOAc. The organic phase was washed with water, dried over anhydrous Na_2SO_4 and concentrated under reduced pressure to afford MMPA.

Synthesis of In_2O_3 NCs

In_2O_3 NCs were synthesized using slight modifications of the literature procedures[42]. Briefly, indium(III) acetate ($In(ac)_3$, 6 mmol), octyl acetate (OctAc, 18 mmol), and OLAM (50 mmol) were dissolved in 50 ml of octyl ether in a three-neck flask. The mixture was degassed under vacuum for 90 min to remove residual oxygen and moisture. Under the N_2 atmosphere, the temperature was raised to 150 °C and held for 1 h to ensure complete reaction of precursors. The solution was then heated to 280 °C and maintained for 2 h to promote NC growth. After cooling to room temperature, the crude product was purified by ethanol precipitation, redispersed in toluene and functionalized by vortex-mixing with a toluene solution of OAm, MMES or MMPA. Excess ligands and byproducts were removed by hexane-induced precipitation. The final In_2O_3 NCs were stored as a homogeneous dispersion in PGMEA.

Perovskite precursor solution

Wide-bandgap $Cs_{0.35}FA_{0.65}PbI_{1.8}Br_{1.2}$ perovskite. The precursor solution (1.4 M) was prepared in mixed solvents of DMF:DMSO:THF with a volume ratio of 3:1:1. The molar ratios for CsI/FAI and $PbI_2/PbBr_2$ were 35:65 and 40:60, respectively. The molar ratio of (CsI + FAI)/(PbI_2 + $PbBr_2$) was 1:1. PEAI (0.5 mol% relative to PbX_2) was added to the precursor solution as the additive. All the salts were dissolved in mixed DMF:DMSO first. The precursor solution was stirred at 50 °C overnight, then filtered through a 0.22 μm polytetrafluoroethylene (PTFE) membrane before use. THF was then added to the filtered DMF:DMSO mixed solution, and the solution was mildly shaken before use.

Narrow-bandgap $FA_{0.7}MA_{0.3}Pb_{0.5}Sn_{0.5}I_3$ perovskite. The molar ratios of FAI/MAI and PbI_2/SnI_2 were 0.7:0.3 and 0.5:0.5, respectively. The molar ratio of (FAI + MAI)/(PbI_2 + SnI_2) was 1:1. Hole-selective material (optimized 0.2 mol% relative to PbI_2 + SnI_2) and SnF_2 (10 mol% relative to SnI_2) were added into the precursor. The solvent ratio of 2-methoxyethanol and tetrahydrofuran to prepare precursor solution (1.4 M) is 4:1. For the precursor preparation (1 ml, for example), 1.4 mmol of above-mentioned salts were first dissolved in 0.8 ml of 2-Me. Then, tin powder (5 mg ml^{-1}) was added as the antioxidant to the precursor solution. DMSO (0.1% mole ratio) as the additive was added to the precursor solution. After all the above additives have been added, the precursor solution was stirred at room temperature for 0.5 h. The precursor solution was filtered through a 0.22 μm PTFE membrane before use. Finally, 0.2 ml of THF was added to the filtered 2-Me-based solution, and the solution was mildly shaken before use. Prolonged stirring of 2-Me-only solution and simultaneous mixing of all components (especially THF) should be avoided, as it may lead to undesirable sedimentation. For the DMF-based perovskite precursor, the same perovskite composition was dissolved in mixed solvents of DMF and DMSO with a volume ratio of 9:1 to obtain the precursor solution (2.4 M).

Narrow-bandgap PSC fabrication

The prepatterned 2.5 × 2.5 cm^2 ITO glass substrates were sequentially cleaned with acetone and IPA. For PEDOT-PSS-based devices, the pristine PEDOT-PSS was dropped on ITO substrates. The blade coater moved at a speed of 10 mm s^{-1}, and the N_2 knife worked at 40 psi during blade coating. Then the substrates were transferred onto a hotplate and annealed at 150 °C for 10 min in air. For In_2O_3 NC-based devices, In_2O_3 NC solution (2 mg ml^{-1}) was blade-coated with a coating gap of 300 μm and a speed of 10 mm s^{-1}, and the N_2 knife worked at 10 psi, followed by annealing at 100 °C for 10 min. After cooling, we transferred the substrates immediately into an N_2-filled glovebox for the deposition of perovskite films. For HTL-free devices, the cleaned ITO glass was directly transferred into the glovebox for perovskite deposition. Perovskite solution (10 μl) was dropped onto the blade coater, which filled the gaps under the influence of gravity and capillary action. For the 2-Me-based solution, the coating speed was 30 mm s^{-1}, with a coating gap of 300 μm. For the DMF-based solution, the coating speed was 6 mm s^{-1}, with a coating gap of 300 μm. Both N_2 knives operated at 60 psi during blade coating. The as-coated films were annealed on one hot plate at 100 °C for 10 min. The post-treatment solution ($EDAI_2$ with a concentration of 0.5 mg ml^{-1} in IPA) was blade-coated on the perovskite films with a coating gap of 200 μm, followed by annealing at 100 °C for 1 min. After cooling down to room temperature, the substrates were transferred to the evaporation system. Then, the 20-nm C_{60} film was subsequently deposited on top by thermal evaporation at a rate of 0.2 Å s^{-1}. The ALD-SnO_2 layer (about 15 nm) was deposited after C_{60} deposition with the process of 0.02 s/6 s/0.02 s/6 s (Sn dose/purge/H_2O dose/purge). Finally, 150 nm Cu films as electrodes were deposited by thermal evaporation at a rate of 1.0 Å s^{-1}.

All-perovskite TSM fabrication

First, we patterned 10 × 10 cm^2 ITO glass substrates for P1 scribing by laser (width 25 μm, 100 W, 1,064 nm, 20 kHz). Then, the patterned ITO substrates were sequentially cleaned using ultrasonication with acetone and isopropanol (IPA) for 30 min, respectively. NiO NCs

were synthesized according to previous reports[20]. NiO NC (5 mg ml^{-1} in deionized water) was blade-coated onto ITO glass substrates at a speed of 10 mm s^{-1}. The N_2 knife operated at 40 psi during blade coating. The gap between the blade coater and the ITO substrate was 200 μm. The substrates were transferred onto a hotplate and annealed at 100 °C for 10 min in air. Then Me-4PACz (0.5 mg ml^{-1} in IPA) was blade-coated onto substrates at a speed of 10 mm s^{-1} and annealed at 100 °C for 10 min in air. Perovskite solution (70 μl) was dropped onto the blade coater, which filled the gaps under the influence of gravity and capillary action. The wide-bandgap perovskite ($Cs_{0.35}FA_{0.65}PbI_{1.8}Br_{1.2}$) precursor solution was blade-coated on the NiO/Me-4PACz-covered ITO glass substrates with a gap of 300 μm at a movement speed of 5 mm s^{-1} in an N_2 glove box. The N_2 knife worked at 60 psi during blade coating. After that, the perovskite films were annealed at 105 °C for 20 min. The post-treatment solution ($EDAI_2$ with a concentration of 0.5 mg ml^{-1}) was blade-coated on the perovskite films with a coating gap of 200 μm, followed by annealing at 100 °C for 1 min. After cooling to room temperature, the substrates were transferred to the evaporation system, and a 20-nm-thick C_{60} film was subsequently deposited on top by thermal evaporation (Beijing Technol Science) at a rate of 0.2 Å s^{-1}. The substrates were then transferred to the ALD system (Veeco Savannah S200) to deposit 20 nm SnO_2 at low temperatures (typically 100 °C) using precursors of tetrakis(dimethylamino) tin(iv) (99.9999%, Nanjing Ai Mou Yuan Scientific Equipment) and deionized water. After ALD deposition, ITO or In_2O_3 NC solution (2 mg ml^{-1}) was blade-coated with a coating gap of 300 μm and a speed of 10 mm s^{-1}, and the N_2 knife worked at 10 psi, followed by annealing at 100 °C for 10 min in air conditions. After the substrates had cooled, we immediately transferred them to an N_2-filled glovebox for the deposition of Pb–Sn perovskite films. Perovskite solution (80 μl) was dropped onto the blade coater, which filled the gaps under the influence of gravity and capillary action. For the 2-Me-based solution, the coating speed was 28 mm s^{-1}, with a coating gap of 300 μm. For the DMF-based solution, the coating speed was 3 mm s^{-1}, with a coating gap of 300 μm. Both the N_2 knives operated at 60 psi during blade coating. The as-coated films were annealed on one hot plate at 100 °C for 10 min. Finally, a 20-nm C_{60} film and a 15-nm ALD-SnO_2 layer were sequentially deposited on perovskite films. The P2 were scribed by laser (width 50 μm, 36.4 μJ, 532 nm, 150 kHz, 500 mm s^{-1}) in air. After P2, the modules were transferred to the ALD system. The conformal diffusion barrier (about 10 nm with 100 cycles ALD-SnO_2) was deposited after P2 as diffusion barrier. Finally, 150 nm Cu films as electrodes were deposited by thermal evaporation at a rate of 1.0 Å s^{-1}. The P3 was also scribed by 532-nm laser in air (width 40 μm, 22 μJ, 532 nm, 200 kHz, 500 mm s^{-1}).

J–*V* and EQE measurement

For single-junction solar cells, the *J*–*V* characteristics were measured using a Keithley 2400 source meter under the illumination of the solar simulator (EnliTech, Class AAA) at a light intensity of 100 mW cm^{-2} as checked with a calibrated reference solar cell (KG-5 and KG-0 reference cells were used for the measurements of WBG and NBG PSCs, respectively). Unless otherwise stated, the *J*–*V* curves were all measured in an N_2-filled glovebox with a scanning rate of 100 mV s^{-1} (voltage steps of 10 mV and a delay time of 100 ms). The active area was determined by the aperture shade masks (0.049 cm^2) placed in front of the solar cells. EQE measurements were performed in ambient air using a QE system (EnliTech) with monochromatic light focused on a device pixel and a chopper frequency of 20 Hz. For tandem solar cells and modules, the *J*–*V* characteristics were carried out under the illumination of a dual-lamp simulator (RAVI SYSTEMS, RHS-220SS) at a light intensity of 100 mW cm^{-2} as checked with calibrated reference solar cells (KG-0). The spectrum from the simulator was finely tuned to ensure that spectral mismatch was within 2% for both subcells. EQE measurements were performed in ambient air, and the bias illumination from highly bright LEDs with emission peaks of 850 nm and 460 nm was used for the measurements of the front subcells and back subcells, respectively. The active area was determined by the aperture shade mask (64.95 cm^2) placed in front of the modules.

Modules encapsulation

The connections were extended by soldering ribbons to the electrodes of the modules. The active area of the module was covered with polyolefin elastomer and edge-sealed with butyl rubber to prevent moisture ingress from the sides of the device. Subsequently, an equally sized encapsulated glass overlaid the entire stack. Finally, vacuum lamination was performed on the stack using an industrial laminator at 110 °C for 20 min. All processes were conducted under ambient air conditions.

Reliability test of modules

The operational stability test was carried out under full AM1.5 G illumination (multi-coloured LED solar simulator, 100 mW cm^{-2}) using a custom-built LabVIEW-based MPP tracking system using a 'perturb and observe' method in ambient conditions with a humidity of 30–50%. The environmental temperature was kept at around 25 °C. The module temperature increased to around 50 °C under illumination as no active cooling was implemented at the measurement stage.

For the damp-heat test, we kept the modules at a closed environmental chamber with fixed temperature (85 °C) and humidity (85% relative humidity) for more than 1,000 h. The encapsulated devices were measured periodically after around 30 min cooling of devices in ambient air.

For the thermal cycling test, the tandem modules were placed in the environmental chamber with temperature cycling between −40 ± 2 °C and +85 ± 2 °C. The rate of change of temperature between the low and high extremes did not exceed 100 °C h^{-1}, and the module temperature remained stable at each extreme for a period of at least 10 min. The whole cycle time was about 6 h, according to the IEC61215:2021 international standard.

The tandem modules were placed on a 65 °C hotplate in ambient conditions. Meanwhile, these modules were exposed to full AM1.5G illumination (multi-coloured LED solar simulator, 100 mW cm^{-2}) while being kept in an open-circuit state for continuous exposure.

Other characterizations

Scanning electron microscopy images were obtained using a TESCAN microscope with an accelerating voltage of 2 kV. X-ray diffraction patterns were collected using a Bruker D2 PHASER diffractometer equipped with an NaI scintillation counter and using monochromatized Cu-Kα radiation (λ = 1.5406 Å). The grazing-incidence X-ray scattering (GI-XRD) data were characterized by the Xeuss SAXS/WAXS 3.0 system with an X-ray wavelength of 1.341 Å (Xenocs). Optical absorption measurements were carried out in a Lambda 1050+ ultraviolet–visible spectrophotometer. Photoluminescence was measured using an FLS980 fluorescence spectrometer (Edinburgh Instruments) with an excitation wavelength of 488 nm. The time-resolved photoluminescence was measured with an excitation wavelength of 600 nm. The photoluminescence decay curves were fitted with biexponential components to obtain fast and slow decay lifetimes. The mean carrier lifetimes τ for the biexponential fit were calculated using the weighted-average method. The photoluminescence imaging tool was an LIS-R1 system sourced from BT Imaging. The samples were excited with a continuous-wave 808 nm laser (one-sun on-sample intensity). The system had a built-in 950 nm long-pass filter to reject the laser light. The camera was a 1,024 × 1,024 pixel, charge-coupled-device silicon detector with a detection range of 400–1,060 nm. The pixel resolution was approximately 162 μm. XPS analysis was carried out using the Thermo Scientific Al K-Alpha XPS system with an energy step of 0.1 eV. Film thickness was measured by Bruker Dektak XT Profiler.

Data availability

All data needed to evaluate the conclusions in the paper are present in the paper or the Supplementary Information.

Author contributions H.T. conceived the idea and directed the overall project. K.X. and H.S. fabricated all the modules and conducted the characterization. H.G. fabricated the devices and performed TRJ characterization. X.K. and Y.W. helped with material synthesis and TEM characteristics. J.L. and C.C. helped with optical-pump terahertz-probe spectroscopy measurement. X.C. and C.M. carried out GIWAXS and UPS measurements. Z.H. and F.F. helped with TAS measurement. R. Lin and R. Liu performed the XRD measurement. D.X., S.X., J.X., Y.L. and X.L. carried out materials characterization. H.T. supervised the project and assisted in data analysis. K.X. wrote the paper. All authors discussed the results and commented on the paper.

Funding This work was financially supported by the National Key R&D Program of China (2022YFB4200304, H.T.), the Natural Science Foundation of Jiangsu Province (BK20232022, BE2022021 and BK20233001, H.T.; BK20251185, H.G.; and BK20232041, Y.W.), the Fundamental and Interdisciplinary Disciplines Breakthrough Plan of the Ministry of Education of China (JYB2025XDXM410, H.T.), the New Cornerstone Science Foundation through the XPLORER PRIZE (H.T.), the National Natural Science Foundation of China (T2325016 and U21A2076, H.T.; 62504100, K.X.; and 52472165, Y.W.), the Technology Innovation Fund of Nanjing University, the Fundamental Research Funds for the Central Universities (0213/14380206 and 0205/14380252, H.T.), the Frontiers Science Center for Critical Earth Material Cycling Fund (DLTD2109, H.T.), the Postdoctoral Innovative Talents Support Project from the China Postdoctoral Science Foundation (BX20230157, K.X.), and the Postdoctoral Innovative Talents Support Project from the China Postdoctoral Science Foundation (BX20240158, H.G.).

Competing interests Three patent applications (CN202610352668.5, CN202411229410.3 and CN202411277886.4) based on this work have been submitted by Nanjing University. H.T. is the founder, chief scientific officer and chairman of Renshine Solar, a company that commercializes perovskite photovoltaics. The other authors declare no competing interests.

Additional information

Supplementary information The online version contains supplementary material available at https://doi.org/10.1038/s41586-026-10768-1.

Correspondence and requests for materials should be addressed to Ke Xiao, Yuanyuan Wang or Hairen Tan.

Peer review information *Nature* thanks Aldo Di Carlo, Junbo Gong and Young Yun Kim for their contribution to the peer review of this work. Peer reviewer reports are available.